Preprints (www.preprints.org) | NOT PEER-REVIEWED | Posted: 27 December 2021 doi:10.20944/preprints202112.0431.v1

Reduction of coil-crack angle sensitivity effect using a novel flux feature of ACFM technique

Ruochen Huang [1], Mingyang Lu [1], Ziqi Chen [1,*] and Wuliang Yin [1]

[1] School of Electrical and Electronic Engineering, University of Manchester, Manchester, M13 9PL, UK
* Correspondence: ziqi.chen@manchester.ac.uk

Abstract: Alternating current field measurement (ACFM) testing is one of promising techniques in the field of non-destructive testing with advantages of the non-contact capability and the reduction of lift-off effects. In this paper, a novel crack detection approach is proposed to reduce the effect of the angled crack (cack orientation) by using rotated ACFM techniques. The sensor probe is composed of an excitation coil and two receiving coils. Two receiving coils are orthogonally placed in the centre of the excitation coil where the magnetic field is measured. It is found that the change of the x component and the peak value of the z component of the magnetic field when the sensor probe rotates around a crack follows a sine wave shape. A customised accelerated finite element method solver programmed in MATLAB is adopted to simulate the performance of the designed sensor probe which can significantly improve the computation efficiency due to the small crack perturbation. The experiments have also been carried out to validate the simulations. It is found that the ratio between the z and x components of the magnetic field remains stable under various rotation angles. It shows the potential to estimate the depth of the crack from the ratio detected by combining the magnetic fields from both receiving coils (i.e., the x and z components of the magnetic field) using the rotated ACFM technique.

Keywords: Non-destructive testing; magnetic induction; crack detection; finite element method acceleration; conductive plate

1. Introduction

Surface crack detection is one of the most essential issues for researchers and engineers to improve the service life of the equipment. A small crack can lead to an unreliable structure which can greatly shorten the service life of the equipment. The techniques developed for the detection of the crack can effectively prevent unnecessary loss and damage. For example, the eddy current (EC) inspection [1-4] and the alternating current field measurement (ACFM) technique [5-7].

Various excitation profiles of the EC inspection have been proposed to quantitively determine the position and size of surface cracks [1-3]. ACFM technique has been originally used in detections of surface cracks in oil and gas industry in previous decades [8-9]. It is capable of inspecting the crack geometries (e.g., depth and length) with high accuracy and elimination of lift-off effects [10-13]. Besides, it enables the sensor probe to detect the surface cracks of metals without removing the coatings. With this feature, it can therefore be successfully applied in the inspection of rail axles which massively saves time and costs. Similar to the EC inspection, both techniques inject the alternating current into the excitation coils resulting in an induced field in the tested material and the receiving coils receive the signals from the induced field. With the presence of the surface crack, the induced eddy current is disturbed so that the crack can be predicted by the received signal. However, in the EC inspection, the impedance of the probe due to the presence of the crack is measured while the (perturbance of) magnetic field is directly measured by the sensor probe in the ACFM [14-15]. The customised finite element method is adopted to simulate the response of the magnetic field due to the crack perturbation. Methods have been proposed to improve the computation efficiency, i.e., using the optimised initial pre-conditioner [16 - 17] and perturbed matrixed inversion [18].

Detection of the surface crack by using the ACFM technique has been developed over the years in order to improve the reliability and sensitivity of the inspection. Sensor probe array has been designed for the inspection [19-20]. A single/multi-layered linear pick-up coil with its electronics, as it is attached below the inducer which generates the high-frequency interrogating field, offers high detection sensitivity (0.5 – 4 mm deep notches) in the inspection of surface cracks for the large metal plates. Theoretically, it can be made in any length, however, the resistance of the circuits limits the length of the sensor [19]. Li et al. proposed a structure of equal-spaced detecting sensors array of the feed-through ACFM probe which can detect the axial crack quantitively and successfully scan the full circumference of the pipe string [20]. Denoising the received signal from the measurements is also crucial to obtain better results of crack information. A magnetic core was appended to the driver coil and the proper wavelet function was chosen to execute the process of de-noise. The signal characteristics were clearer after denoising by using the wavelet function [21].

Moreover, inverse problems for estimating the geometry information of the surface crack in the workpiece have been used in the ACFM techniques. Ravan et al. presented the method based on the artificial neural network scheme which can be used to predict the depth of surface cracks with random geometry and known length and direction of crack. However, the accuracy of depth prediction depends on the level of noise from the measurement data [22]. Fuzzy rules are also popularly applied in the identification of the crack [12, 23-24]. Noroozi et al. utilised the fuzzy alignment algorithm (FAA) to effectively map the depth of the crack to the signal output from the probe. The FAA is capable to diminish the impact aroused by the irrelevant training data and converged efficiently by setting a degree of the freedom to manipulate the influence from the dataset. This method shows a good performance for the crack with arbitrary crack shape [12]. These methods require a certain amount of computation and it is common to obtain the direction of the crack using the 2D scanning technique in advance.

During the measurement process, the vibration of the experiment setup would affect the accuracy of the measurement, leading to unnecessary damage. Gu et al. proposed a structural optimization method and an absorber was used to reduce the vertical vibration of the machine [25]. Without knowing the crack orientation, the angle between the crack and the sensor probe would influence quantifying the crack dimension. In this paper, to analysis and reduce the effect of the angled coil (compared to the crack orientation) above the surface crack on conductive metals, a crack detection method by utilising rotated ACFM technique is proposed. For the proposed method, the designed sensor probe scans above the sample plate in different angles. By using this method, the angle between the crack and the sensor probe can be eliminated. Simulations are conducted in the customised accelerated finite-element solver programmed in MATLAB and experiments have been carried out to verify the proposed features.

2. Relationship between the measured magnetic field and the rotation angle

2.1 Magnetic field calculated by the accelerated finite element analysis

As a versatile computation technique of simulating electromagnetic problems, finite element method (FEM) is widely applied in diverse industrial applications in non-destructive testing. With the support of A-V Edge-Element Formulation, FEM simulation was set up in MATLAB and by using the generated sample model, the magnetic field can be computed. In the formulation, Galerkin method is employed to compute the vector potential ($\boldsymbol{A}$) and scalar potential (V) of the whole domain [18]. The vector and scalar potentials in individual element satisfy:

Preprints (www.preprints.org) | NOT PEER-REVIEWED | Posted: 27 December 2021 doi:10.20944/preprints202112.0431.v1

$$\int_{\Omega_c} \nabla \times N_i \cdot v \nabla \times \boldsymbol{A}^n d\Omega + \int_{\Omega_c} j\omega\sigma N_i \cdot \boldsymbol{A}^n d\Omega + \int_{\Omega_c} j\omega\sigma N_i \cdot \nabla V^n d\Omega = \int_{\Omega_c} \nabla \times N_i \cdot v_0 \nabla \times \boldsymbol{A}_s \, d\Omega \quad i = 1,2,\ldots,6 \tag{1}$$

$$\int_{\Omega_c} j\omega\sigma \nabla L_i \cdot \boldsymbol{A}^n d\Omega + \int_{\Omega_c} j\omega\sigma \nabla L_i \cdot \nabla V^n d\Omega = 0 \quad i = 1,2,\ldots,4 \tag{2}$$

Where: N_i is the edge interpolation function in ith edge; L_i is the nodal interpolation function in ith edge; Ω_c is the metallic domain in the sample model; v is the sample reluctivity; σ is the sample conductivity; v_0 denotes the reluctivity in air.

For each tetrahedral element, the interpolation functions are unique so that transformation of the coordinates is used to transform the global coordinates (λ_v, λ_s) to the local coordinates $(\hat{\lambda}_v, \hat{\lambda}_s)$. In consequence, the interpolation functions can be given [18]

$$J = \begin{bmatrix} \frac{\partial x}{\partial \xi} & \frac{\partial y}{\partial \xi} & \frac{\partial z}{\partial \xi} \\ \frac{\partial x}{\partial \eta} & \frac{\partial y}{\partial \eta} & \frac{\partial z}{\partial \eta} \\ \frac{\partial x}{\partial \zeta} & \frac{\partial y}{\partial \zeta} & \frac{\partial z}{\partial \zeta} \end{bmatrix} \tag{3}$$

$$\lambda_v = J^{-1}\hat{\lambda}_v \tag{4}$$

$$\lambda_s = J^{-1}\hat{\lambda}_s \tag{5}$$

$$\nabla \times \lambda_v = \frac{1}{|J|} J^T \nabla \times \hat{\lambda}_v \tag{6}$$

Where, J is the Jacobian matrix, λ_v is the vector component in the global coordinates, λ_s is the scalar component in the global coordinates, $\hat{\lambda}_v$ is the vector component in the local coordinates, $\hat{\lambda}_s$ is the scalar component in the local coordinates.

Therefore, employing equations (1) and (2), a linear algebraic system equation can be expressed by using the stiffness matrix Q.

$$Q = \begin{bmatrix} K^{p\times p} & L^{p\times q} \\ M^{q\times p} & N^{q\times q} \end{bmatrix} \tag{7}$$

$$Q \begin{bmatrix} \begin{bmatrix} \boldsymbol{A}_1 \\ \vdots \\ \boldsymbol{A}_p \end{bmatrix} \\ \begin{bmatrix} V_1 \\ \vdots \\ V_q \end{bmatrix} \end{bmatrix} = X \tag{8}$$

Here, p is the edge number, q is the vertex node number. K, which is associated to the summation of the first two terms of equation (1), mainly dominates by the vector field and contributes to the generation of the vector potential. L is the third term of equation (2), controlling the flow of the eddy current as it encounters with the notch. M and N are the terms of left-hand side of equation (2), satisfying the conditions of magnetostatic field. X is the terms of right-hand side of equation (1) and (2), providing the background field of the entire system.

In order to hasten the computation speed, the accelerated method based on the property that the crack only disturbs its surrounding field is adopted [26]. In this method, the stiffness matrix Q can be rearranged and divided into four parts, Q_1, Q_2, Q_3 and Q_4. Here Q_1 is the matrix unaffected by the small perturbation while Q_2, Q_3 and Q_4 are the matrices affected by the small perturbation. S_u and S_c are the field solution of the unaffected domain and affected domain respectively. X_u and X_c are the background field of the unaffected domain and affected domain. The system matrix equation turns to

$$\begin{bmatrix} Q_1 & Q_2 \\ Q_3 & Q_4 \end{bmatrix} \begin{bmatrix} S_u \\ S_c \end{bmatrix} = \begin{bmatrix} \begin{bmatrix} K_1 & L_1 \\ M_1 & N_1 \end{bmatrix} & \begin{bmatrix} K_2 & L_2 \\ M_2 & N_2 \end{bmatrix} \\ \begin{bmatrix} K_3 & L_3 \\ M_3 & N_3 \end{bmatrix} & \begin{bmatrix} K_4 & L_4 \\ M_4 & N_4 \end{bmatrix} \end{bmatrix} \begin{bmatrix} \begin{bmatrix} \boldsymbol{A}_u \\ V_u \end{bmatrix} \\ \begin{bmatrix} \boldsymbol{A}_c \\ V_c \end{bmatrix} \end{bmatrix} = \begin{bmatrix} X_u \\ X_c \end{bmatrix} \tag{9}$$

Then due to the perturbation of the small crack, crack matrices are introduced, the system is equal to

Preprints (www.preprints.org) | NOT PEER-REVIEWED | Posted: 27 December 2021 doi:10.20944/preprints202112.0431.v1

$$\begin{bmatrix} Q_1 & Q_2+\Delta Q_2 \\ Q_3+\Delta Q_3 & Q_4+\Delta Q_4 \end{bmatrix}\begin{bmatrix} S_u{}' \\ S_c{}' \end{bmatrix}=\begin{bmatrix} X_u \\ X_c \end{bmatrix} \tag{10}$$

By utilising the fact that the perturbed field due to the crack can be localised to its surrounding area, the solutions can be obtained by equation (11) which can effectively hasten the computation speed [26].

$$\begin{cases} S_u{}' = S_u \\ (Q_4+\Delta Q_4)S_c{}' = X_c-(Q_3+\Delta Q_3)S_u \end{cases} \tag{11}$$

Therefore, after obtaining the magnetic vector potential field $\boldsymbol{A}_p$ along all the edges and electric scalar potential field V_q on all the vertex of the entire crack system, the eddy current produced in the tested sample is equal as

$$J_s = \sigma E = -j\omega\sigma\boldsymbol{A} - \sigma\nabla V \tag{12}$$

Where, E is the electric field contributed by both the vector and scalar potential field. Based on the Biot-Savart law, the magnetic $\boldsymbol{B}$ field can be derived as

$$\boldsymbol{B} = \frac{\mu_0}{4\pi}\int\frac{J_s \times r'}{|r'|^3}dV \tag{13}$$

Here μ_0 denotes the permeability in the vacuum, J_s denotes the generated eddy current in the tested sample and r' denotes the displacement vector from the current element to the computed point. Consequently, Bx and Bz can be described by the first and third components of the calculated magnetic B field and the ratio between Bz and Bx can be calculated.

2.2 Simulation models

Figure 1 shows the rotation direction of the sensor probe (rotates counter-clockwise) and it scans above the non-magnetic tested sample with/without the crack. As shown in Table 1, the height and the length of the excitation coil were set to 3 mm and 4 mm respectively. The radius of the receiving coils is 0.5 mm. The probe was placed 0.5 mm above the sample model. The conductivity of the sample plate is 1.4 MS/m with the length of 75 mm and the width of 40 mm. The thickness of the sample in the model is 2 mm and the length and width of the crack in the centre of the plate are 10 mm and 0.25 mm respectively.

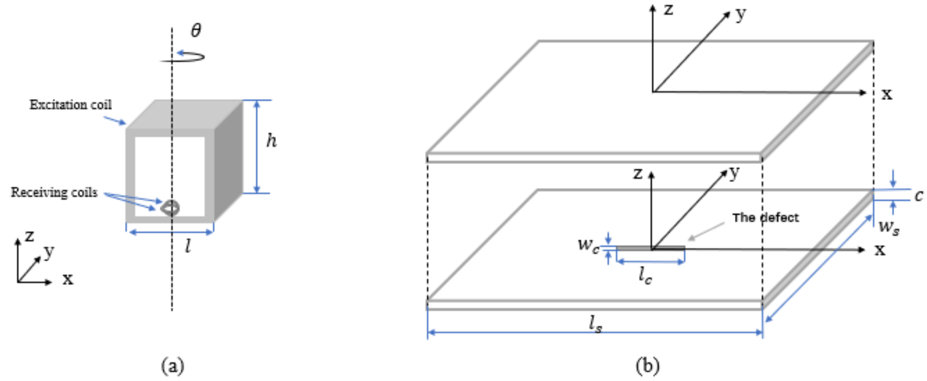

Figure 1. Simulation models (a) the rotation direction of the sensor probe (b) the stainless-steel plate with/without the crack.

Table 1. Model parameters

	Values
Height of excitation coil h (mm)	3
Length of excitation coil l (mm)	4
Turns of excitation coil N_e	5
Radius of receiving coils r_p (mm)	0.5
Turns of receiving coils N_p	1
Lift-off l_o (mm)	0.5
Width of the sample plate w_s (mm)	75
Length of the sample plate l_s (mm)	40

Thickness of the sample plate c (mm)	2
Width of the crack w_c (mm)	10
Length of the crack l_c (mm)	0.25
Conductivity of the sample plate σ (MS/m)	1.4

2.3 Eddy currents around cracks using the FEM solver

The behaviour of the eddy current around the crack on the sample plate is simulated using the accelerated FEM solver. The sensor probe is situated above the centre of the sample plate with different rotation angles and the lift-off of 0.5 mm. Fig. 2 shows the vector diagram of the eddy current flow under three rotation angles, $0^{\circ}, 45^{\circ}$ and 90° respectively.

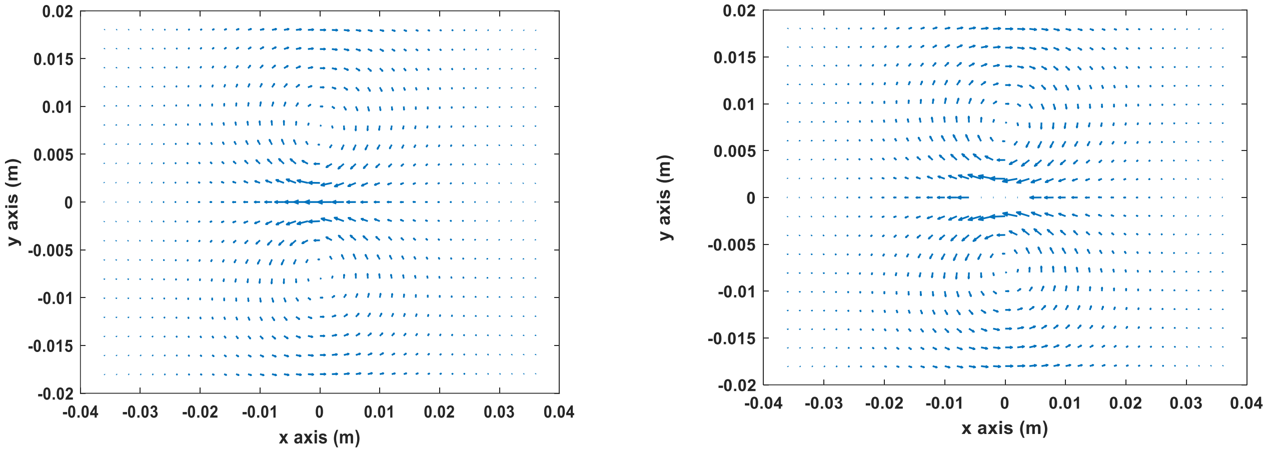

(a)

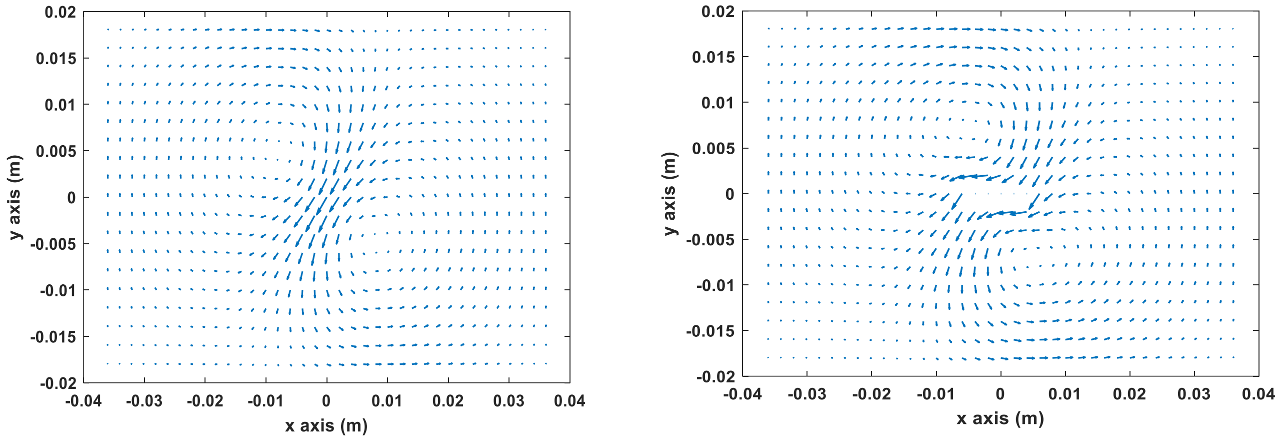

(b)

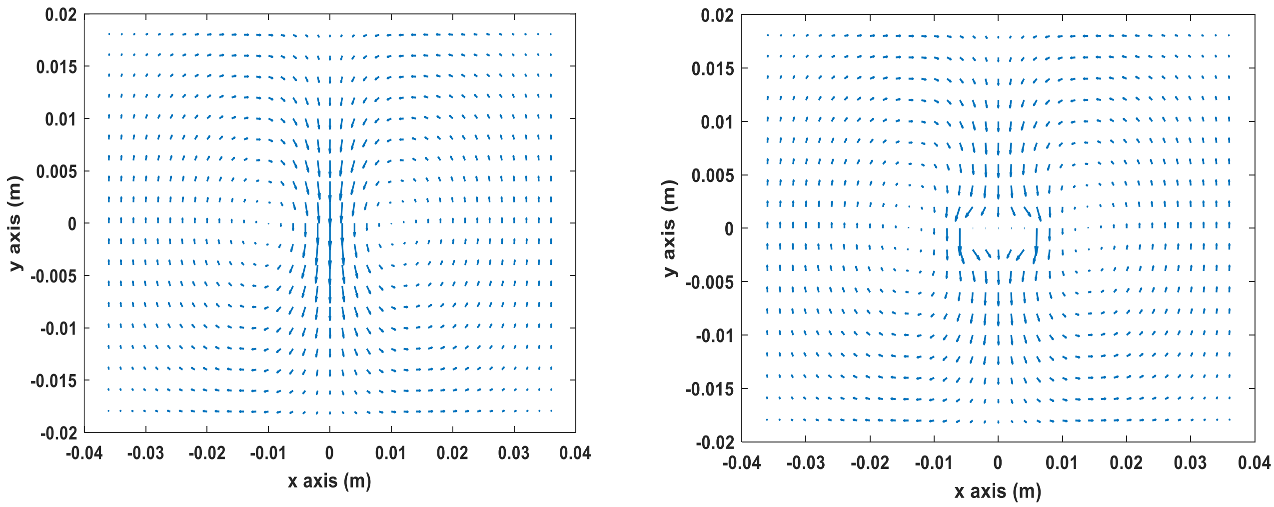

(c)

Figure 2. The flow of eddy current induced on the non-magnetic tested sample without/with the crack (a) rotation angle 0° (b) rotation angle 45° (c) rotation angle 90°.

As shown in Fig. 2, it can be noted that the eddy current distributed uniformly in the centre of the sample plate and has the feature of symmetry. The eddy current flows uniformly and continuously in the sample plate without the disturbance of the crack. When the eddy current encounters with a crack, it will flow around the edge of the crack. As can be seen in Fig. 2(a), when the sensor probe is parallel to x axis (rotation angle 0°), the eddy current is hardly affected, then the probe rotates to 45°, the eddy current is perturbed and flows according to the geometry of the crack. The strongest perturbation occurs when it rotates to 90^{o}, shown in Fig. 2(c). Consequently, the impact to the eddy current due to the crack for the sensor probe perpendicular to x axis (rotation angle 90°) is strongest compared with other rotation angles, resulting in the significant change of the magnetic field. Due to the rotation of the sensor probe, the strength of the detected magnetic field is affected by the induced eddy currents varies. Therefore, it can be deduced that the weakest appears at the angle of $0^{\circ}/180^{\circ}$ and the strongest appears at the angle of 90°.

2.4 Coil angle-immune feature on crack detection using the rotary sensor probe

To simulate the magnetic field due to the presence of the crack in the sample model, the sensor probe scans across the crack along x axis from (-20, 0, 0.5) mm to (20, 0, 0.5) mm (i.e., perpendicularly to the crack - rotation angle 90°). The model parameters listed in Table 1 were kept the same in the process of the entire simulation. Considering the effect of different depths, the crack in the centre was evenly divided into 10 layers, from 0.2 mm to 2 mm. Fig. 3 shows the received magnetic B field with different excitation frequencies. From the simulations, the response of the sensor probe is more evident to see the changes of the magnetic B field using higher excitation frequency. Besides, since the maximum depth of the crack is 2 mm, in order to have a better performance of crack detection, it is better to make sure the skin depth of the eddy current to be larger than 2 mm (< 45 kHz for the conductivity of 1.4 MS/m), therefore, the frequency was chosen to be 20 kHz.

Preprints (www.preprints.org) | NOT PEER-REVIEWED | Posted: 27 December 2021 doi:10.20944/preprints202112.0431.v1

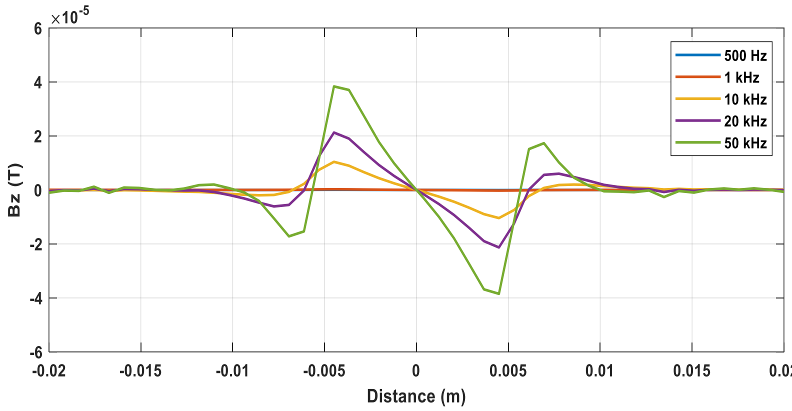

(a)

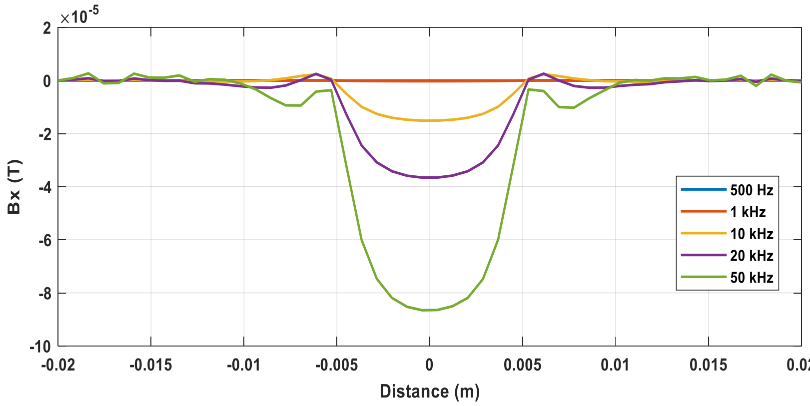

(b)

Figure 3. The magnetic B field received by the sensing probe under different excitation frequencies (a) Bz (b) Bx.

Fig. 4 illustrates the x and z components of the magnetic B field caused by the cracks with different depths varying from 1 mm to 2 mm under the excitation frequency of 20 kHz. It can be seen that, in the centre of the crack, the z component of the magnetic B field is zero while the x component of the magnetic B field reaches the minimum value. It can be observed that, the deeper the crack, the larger the peak value of Bz and Bx.

Further, the sensor probe scans across the crack with a range of rotation angles starting from 15 degree (one period) in steps of 15 degrees to investigate the variation of the two components of the magnetic field. Fig. 5(a) depict the variations of the maximum value of Bz and the difference of Bx with the changing rotation angle. It can be noticed that the trend of the peak value of Bz and the difference of Bx is similar. Both of them increase at the beginning, then reach its maximum at the angle of 90o and decrease again. They follow a sine relationship between the rotation angle and the x/z component of the magnetic B field. As can be seen from Fig. 5(b), the ratio of the maximum of the z component (Bz) and the change of the x component (Bx) stays constantly under a range of angles. It can be noted that the ratio is nearly immune to the rotation angle with reasonable variation (3%) and the value increases under different depths of the crack. Besides, when the centre of receiving coils is not overlapped (i.e. the receiving coil for detecting x component of the magnetic B field is placed with higher lift-off, above the receiving coil for detecting z component of the magnetic B field), the ratio increases from 0.54 to 0.83, shown in Fig. 6. The reason of the increase of the ratio is because that, with higher lift-off of the receiving coil for detecting x component of the magnetic B field, the difference of Bx becomes smaller so that the ratio increases but still remains stable under varying rotation angles. It shows the potential of using this ratio to determine the depth of the crack by reducing the effect of the crack orientation.

Preprints (www.preprints.org) | NOT PEER-REVIEWED | Posted: 27 December 2021 doi:10.20944/preprints202112.0431.v1

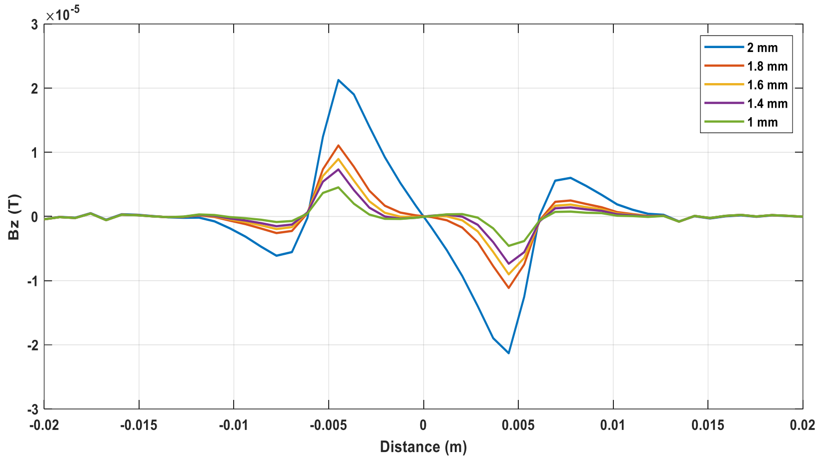

(a)

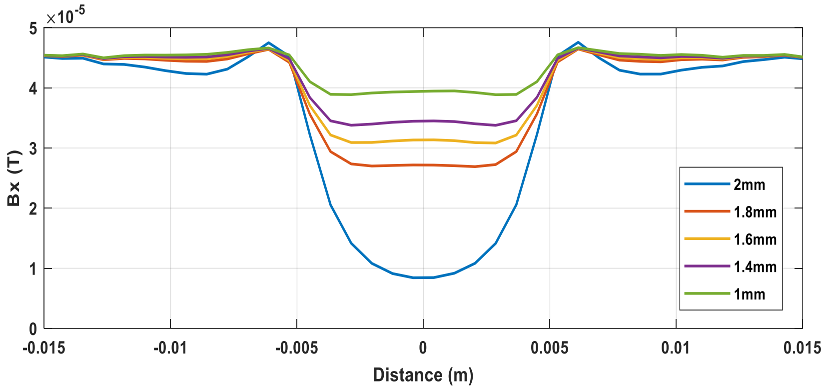

(b)

Figure 4. The magnetic B field signal received by the sensing probe under different depths of the cracks (a) Bz (b) Bx.

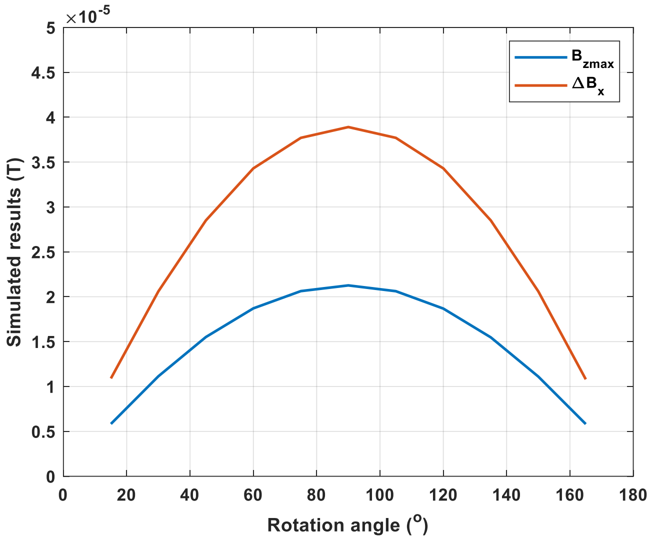

(a)

Preprints (www.preprints.org) | NOT PEER-REVIEWED | Posted: 27 December 2021 doi:10.20944/preprints202112.0431.v1

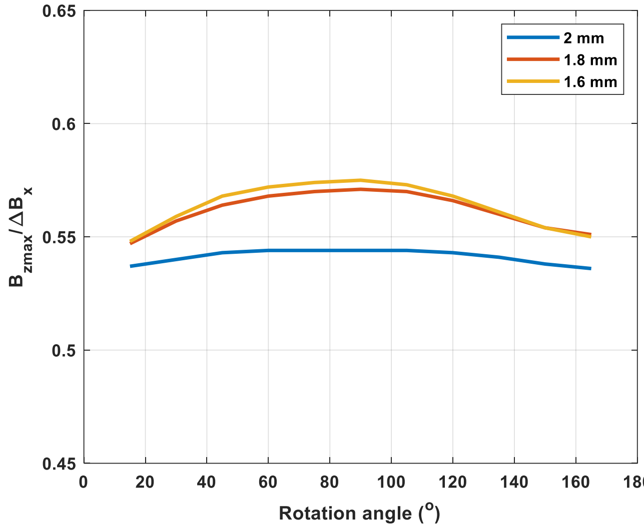

(b)

Figure 5. (a) The simulated results of the B magnetic field for the crack depth of 2 mm (b) The ratio of the maximum of the z component and the change of the x component under varying rotation angles for different crack depths.

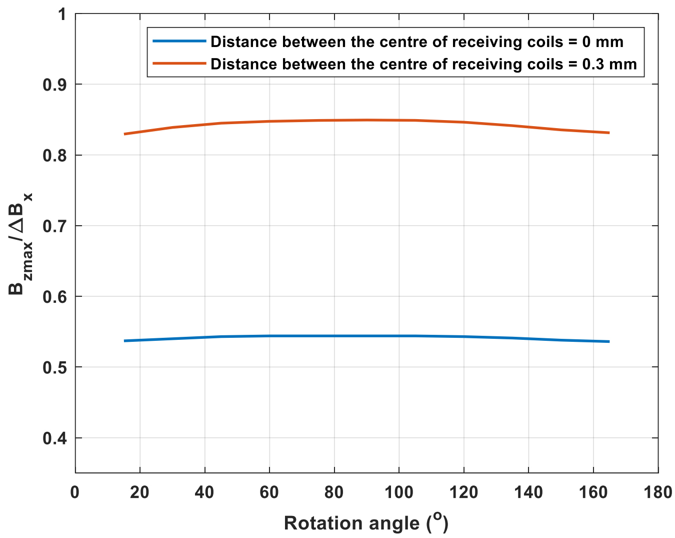

Figure 6. The ratio of the maximum of the z component and the change of the x component under varying rotation angles for different distance between the centre of receiving coils with the crack depth of 2 mm.

3. Experiments

3.1 Experimental setup

Fig. 7 shows the experiment setup for crack detection, consisting of a stepper, the electromagnetic (EM) instrument, host PC, sensor probe and the sample plate. The sensor probe is attached to the stepper, whose movements in different axis can be controlled by the host PC to perform scanning process. The sample plate is fixed at the stage and the sensor probe is right on the top of the cracks during scanning. The experiment parameters are listed in Table 1. The magnetic field is detected by the EM instrument developed by the Sensing, Imaging and Signal Processing group at the University of Manchester [27-28].

The EM instrument is based on field programmable gate array (FPGA) programming which enables its high speed for the detecting process. As shown in Fig. 1(a), the excitation coil is vertically placed above the sample plate (lift-off of 1.5 mm) with 20 turns. The length and height of the excitation coil are 12 mm and 10 mm respectively. As is shown in Fig.1 and Fig.8, two receiving coils are assembled in the centre of the excitation coil along the x-axis and the z-axis respectively for detecting the z and x components of the magnetic B field. The radius and turns of the receiving coil are 0.8 mm and 200 respectively. The stainless steel sample plate is used which contains 20 small cracks with the length of 10 mm and the width of 0.25 mm. The depth of the crack is from 0.1 mm to 2 mm, with an increasing step of 0.1 mm.

During the scanning process, the sensor probe moves right on the top of the crack along the x-axis, which performs line scanning. The trajectory of the sensor probe covers the total length of the crack. In Fig.8, the angle between the excitation coil and the x-axis is 90° and a maximum B_x can be detected. During the experiments, the sensor probe was rotated and line scanning was performed at different angle. In Fig.9, the orientation of the sensor probe at 0° and 90° is demonstrated respectively. The direction of the induced magnetic field varies with the orientation of the excitation coil, which results in different level of change in the measurements at each angle.

The measured results are presented by the difference of the received voltage of the sample with the crack and without the crack. As shown in Fig. 10, the excitation frequency from 10 kHz to 60 kHz is used for testing the crack with a depth of 2 mm. It can be noted that frequency ranges from 20 kHz to 50 kHz works well and have a better SNR. Therefore, 20 kHz was selected as the excitation frequency. Besides, the excitation frequency of 20 kHz works for different depths of crack is shown in Fig. 11 and it can be noticed that there is a rising trend of the peak-to-peak value of z component of the magnetic field as the crack depth increases.

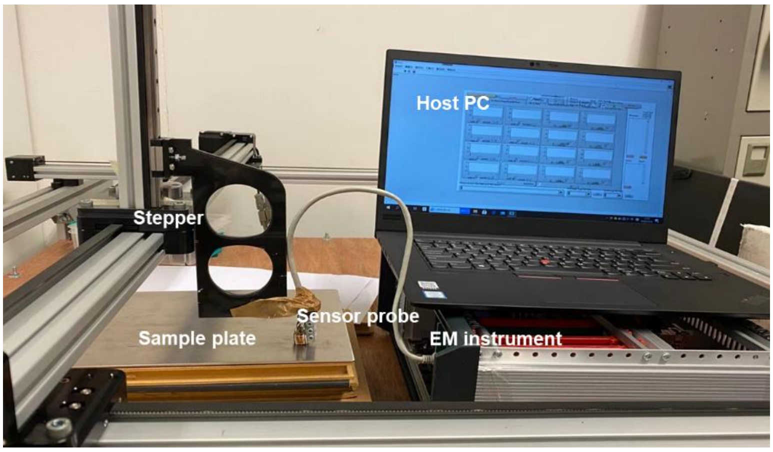

Figure 7. Experimental setup.

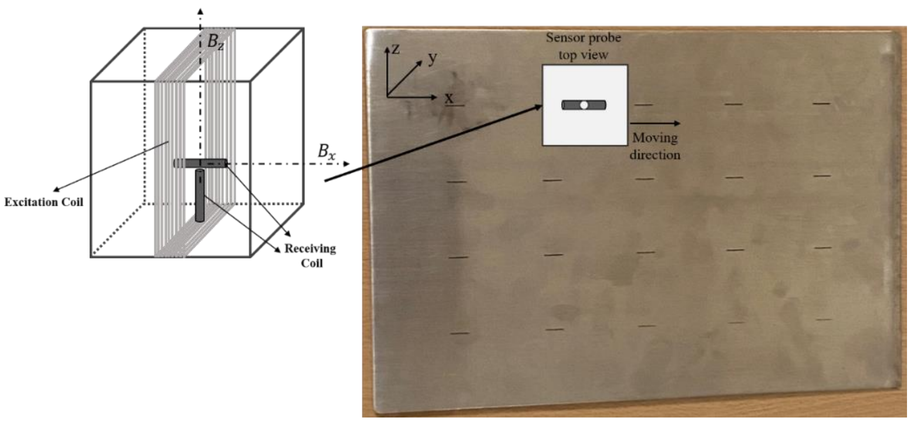

Figure 8. The trajectory of the sensor probe.

Preprints (www.preprints.org) | NOT PEER-REVIEWED | Posted: 27 December 2021 doi:10.20944/preprints202112.0431.v1

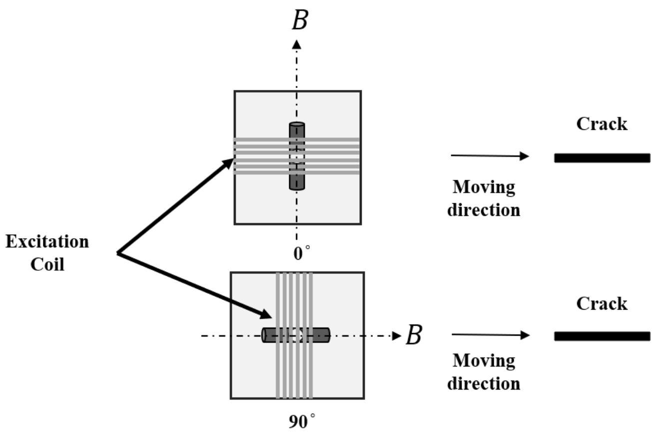

Figure 9. The orientation of the sensor probe at 0° and 90°.

Table 2. Experimental parameters.

Excitation coil	Length (mm)	12
	Height (mm)	10
	Turns	20
Receiving coil	Radius (mm)	0.8
	Turns	200
Loft-off (mm)		1.5
Excitation frequency (kHz)		20
Crack depth (mm)		0.1 : 0.1 : 2

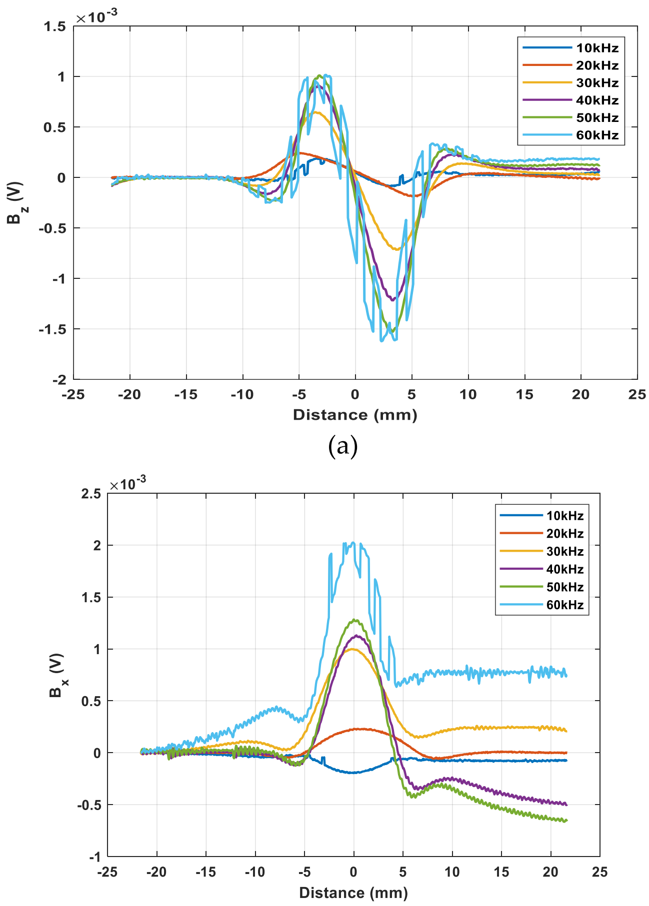

(a)

(b)

Figure 10. The voltage received from the sensor probe under different frequencies (a) Bz (b) Bx.

Preprints (www.preprints.org) | NOT PEER-REVIEWED | Posted: 27 December 2021 doi:10.20944/preprints202112.0431.v1

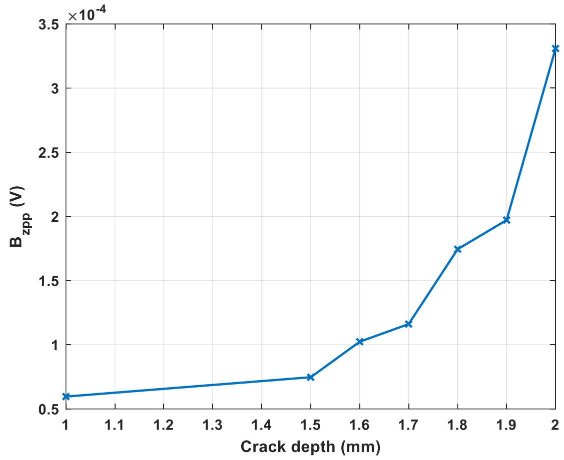

Figure 11. The peak-to-peak value of z component of the magnetic field with different crack depths under the frequency of 20 kHz.

3.2 Coil-crack angle insensitive feature

As can be seen in Fig. 12, the trend of the magnetic field under different rotation angles is similar compared with the simulation results. Fig. 13 shows the received maximum value of the z component and the change of x component of the magnetic B field with a range of rotation angles. The value of the x and z components of the magnetic B field increases with the rotation angle from 15º, reaching maximum when the rotation angle is 90º. This is because more eddy current is blocked (flowing route is influenced) due to the presence of the crack as the sensor probe rotates vertically to the crack. Then continue to rotate the sensor probe, the value reversely decreases to reach its minimum. They agreed with the simulated results which are symmetric with respect to 90º. Moreover, it can be seen in Fig. 13 (b) that there is a coil angle immune feature for the ratio of the maximum of Bz and the change of Bx when the sensor probe scans the crack on the surface of the metal. Due to the measurement error and the environments, there is a small fluctuation for the ratio but most of them are mainly around 0.8, which are consistent with the simulated results. Besides, it also shows that the position of the receiving coil for detecting x component of the magnetic B field does not influence the coil-crack angle insensitive feature. Therefore, the effect caused by the coil-crack angle can be eliminated by the feature and may useful to estimate the depth of the crack without the disturbance of the crack orientation.

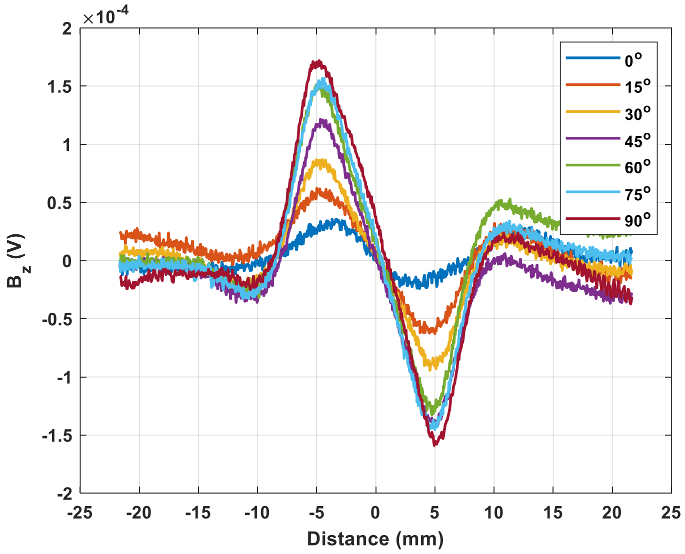

(a)

Preprints (www.preprints.org) | NOT PEER-REVIEWED | Posted: 27 December 2021 doi:10.20944/preprints202112.0431.v1

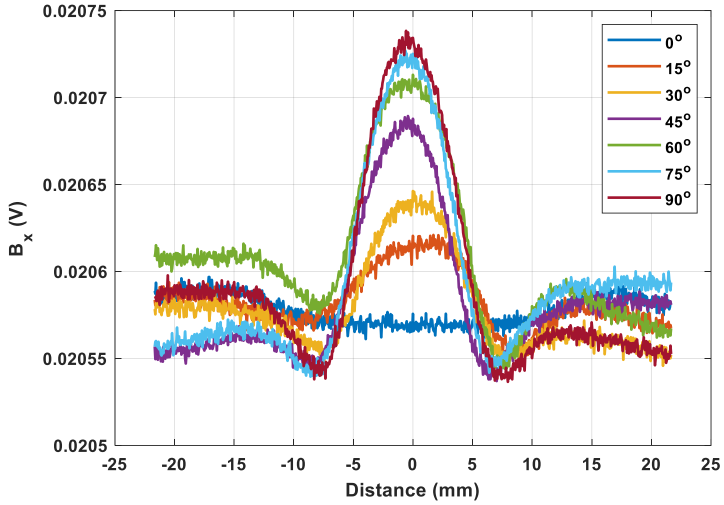

302

(b) 303

Figure 12. The measurement results of the magnetic field under the rotation angle from 0o to 180o 304
(a) the z component (b) the x component. 305

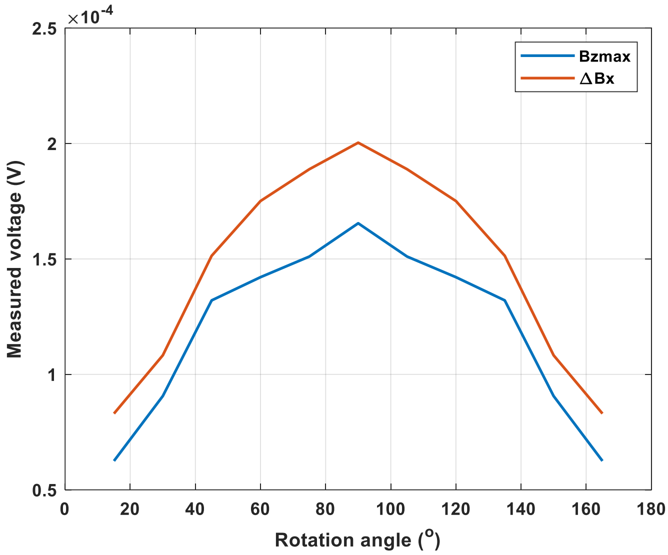

306

(a) 307

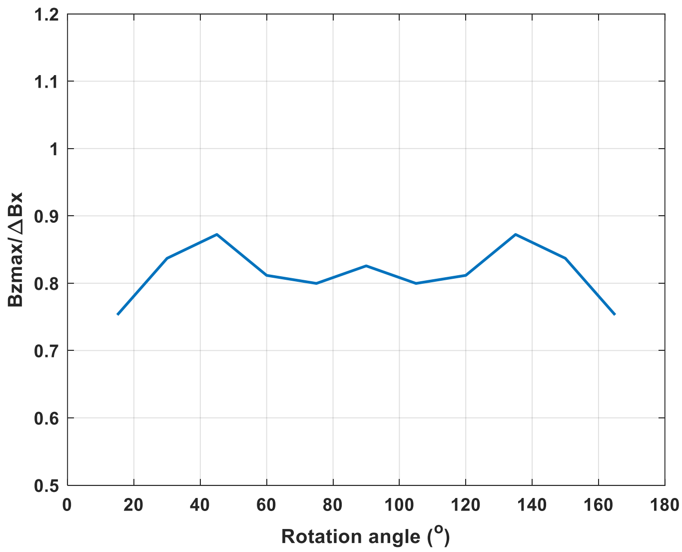

308

(b) 309

Figure 13. (a) The measured results of the B magnetic field (b) The ratio of the maximum of the z 310
component and the change of the x component under varying rotation angle. 311

4. Conclusions

In this paper, a novel crack detection method by using rotated ACFM techniques is proposed. The proposed method is using the sensor probe with two orthogonal receiving coils to detect the magnetic B field under different rotation angles. It is found that there is a sine relationship between the peak value of the z component / the change of the x component of magnetic B field and the rotated angle. Besides, it is noted that the ratio of peak value of the z component and the change of x component stays constantly under different rotation angles. It also validated by the measurement results. By utilising this feature, it may be used to determine the depth of the crack reducing the effect of the crack orientation for conductive metallic plate. Moreover, with the support of the proposed method, it simplifies the sensor setup with low cost.

Author Contributions: Conceptualization, R.H. and W.Y.; methodology, R.H. and M.L.; software, R.H.; validation, R.H., M.L. and Z.C; formal analysis, R.H.; data curation, R.H. and Z.C.; writing—original draft preparation, R.H.; writing—review and editing, R.H., M.L. and W.Y.; supervision, W.Y. All authors have read and agreed to the published version of the manuscript.

Funding: This work was supported by the U.K. Engineering and Physical Sciences Research Council through the project [Real-time In-line Microstructural Engineering (RIME)] under Grant EP/P027237/1 and the UK Research Centre in Non-Destructive Evaluation (RCNDE) under contract EP/L022125/1.

Conflicts of Interest: The authors declare no conflict of interest.

References

1. Ye, C.; Rosell, A.; Haq, M.; et al. EC probe with orthogonal excitation coils and TMR sensor for CFRP inspection. International Journal of Applied Electromagnetics and Mechanics, 2019, 59(4): 1247-1255.
2. Xu, Z.; Wang, X; Deng, Y.; Rotating focused field Eddy-current sensing for arbitrary orientation defects detection in carbon steel. Sensors, 2020, 20(8): 2345.
3. Ye, C; Huang, Y.; Udpa, L.; et al. Novel rotating current probe with GMR array sensors for steam generate tube inspection. IEEE Sensors Journal, 2016, 16(12): 4995-5002.
4. Yang, G.; Dib, G.; Udpa, L.; et al. Rotating field EC-GMR sensor for crack detection at fastener site in layered structures. IEEE Sensors Journal, 2014, 15(1): 463-470.
5. Knight, M J.; Brennan, F. P.; Dover, W. D.; Effect of residual stress on ACFM crack measurements in drill collar threaded connections. Ndt & E International, 2004, 37(5): 337-343.
6. Low, C. K.; Wong, B. S.; Defect evaluation using the alternating current field measurement technique. Insight-Non-Destructive Testing and Condition Monitoring, 2004, 46(10): 598-605.
7. Blakeley, B.; Lugg, M.; ACFM: Application of ACFM for inspection through metal coatings. Insight-Non-Destructive Testing and Condition Monitoring, 2010, 52(6): 310-315.
8. Raine, G. A.; Smith, N.; NDT of on and offshore oil and gas installations using the alternating current field measurement (ACFM) technique. Materials evaluation, 1996, 54(4).
9. Lugg, M. and Topp, D. Recent developments and applications of the ACFM inspection method and ACSM stress measurement method. In Proceedings of ECNDT, 2006, Berlin, Germany, 2006.
10. Raine, A.; Lugg, M. A review of the alternating current field measurement inspection technique. Sensor Review, 1999.
11. Gaynor, T M.; Roberts, D. L.; Homan, E.; et al. Reduction in fatigue failures through crack detection by alternating current field measurement. IADC/SPE drilling conference. OnePetro, 1996.
12. Noroozi, A.; Hasanzadeh, R. P. R.; Ravan, M. A fuzzy learning approach for identification of arbitrary crack profiles using ACFM technique. IEEE Transactions on Magnetics, 2013, 49(9): 5016-5027.
13. Howitt, M. Bombardier brings ACFM into the rail industry. Insight, 2002, 44(6): 379-382.
14. Shen, J. Responses of alternating current field measurement (ACFM) to rolling contact fatigue (RCF) cracks in railway rails. University of Warwick, 2017.
15. Dover, W. D.; Collins, R.; Michael, D. H. Review of developments in ACPD and ACFM. British Journal of Non-Destructive Testing, 1991, 33(3): 121-127.
16. Yin, W.; Lu, M.; Yin, L.; et al. Acceleration of eddy current computation for scanning probes. Insight-Non-Destructive Testing and Condition Monitoring, 2018, 60(10): 547-555.
17. Lu, M.; Peyton, A.; Yin, W. Acceleration of frequency sweeping in eddy-current computation. IEEE Transactions on Magnetics, 2017, 53(7): 1-8.
18. Huang, R.; Lu, M.; Peyton, A.; et al. A novel perturbed matrix inversion based method for the acceleration of finite element analysis in crack-scanning eddy current NDT. IEEE Access, 2020, 8: 12438-12444.

19. Mirshekar-Syahkal, D. and Mostafavi, R. F. 1-D probe array for ACFM inspection of large metal plates. IEEE transactions on instrumentation and measurement, 2002, 51(2): 374-382.
20. Li, W.; Chen, G.; Yin, X.; et al. A feed-through ACFM probe with sensor array for pipe string cracks inspection. Ndt & E International, 2014, 67: 17-23.
21. Ren, S.; Zhu, Z.; Lin, T.; et al. Design for the acfm sensor and the signal processing based on wavelet de-noise. 2009 2nd International Congress on Image and Signal Processing. IEEE, 2009: 1-4.
22. Ravan, M.; Sadeghi, S. H. H.; Moini, R. Neural network approach for determination of fatigue crack depth profile in a metal, using alternating current field measurement data. IET Science, Measurement & Technology, 2007, 2(1): 32-38.
23. Sinha, S. K.; Fieguth, P. W. Neuro-fuzzy network for the classification of buried pipe defects. Automation in Construction, 2006, 15(1): 73-83.
24. Pawar, P. M.; Ganguli, R. Matrix crack detection in thin-walled composite beam using genetic fuzzy system. Journal of Intelligent Material Systems and Structures, 2005, 16(5): 395-409.
25. Gu, Z.; Chen, M.; Wang, C.; et al. Static and Dynamic Analysis of a 6300 KN Cold Orbital Forging Machine. Processes, 2021, 9(1): 7.
26. Huang, R.; Lu, M.; Chen, Z.; et al. A novel acceleration method for eddy current crack computation using finite element analysis. Ndt & E International, 2021 (Under review).
27. Xu, H.; Lu, M.; Avila, J. R.; et al. Imaging a weld cross-section using a novel frequency feature in multi-frequency eddy current testing. Insight-Non-Destructive Testing and Condition Monitoring, 2019, 61(12): 738-743.
28. Avila, J. R. S.; Chen, Z.; Xu, H.; et al. A multi-frequency NDT system for imaging and detection of cracks. 2018 IEEE International Symposium on Circuits and Systems (ISCAS). IEEE, 2018: 1-4.
29. Lu, M.; Meng, X.; Huang, R.; Peyton, A.; Yin, W. Analysis of Tilt Effect on Notch Depth Profiling Using Thin-Skin Regime of Driver-Pickup Eddy-Current Sensor. Sensors **2021**, 21(16), 5536. https://doi.org/10.3390/s21165536
30. Lu, M.; Xu, H.; Zhu, W.; Yin, L.; Zhao, Q.; Peyton, A.; Yin, W. Conductivity Lift-off Invariance and measurement of permeability for ferrite metallic plates. NDT & E International, 2018, 95, 36-44.
31. Lu, M.; Peyton, A.; Yin, W. Acceleration of frequency sweeping in eddy-current computation. IEEE Transactions on Magnetics, 2017, 53, 1-8.
32. Avila, J.R.S.; Lu, M.; Huang, R.; Chen, Z.; Zhu, S.; Yin, W. Accurate measurements of plate thickness with variable lift-off using a combined inductive and capacitive sensor. NDT & E International, 2020, 110, 102202.
33. Lu, M.; Meng, X.; Yin, W.; Qu, Z.; Wu, F.; Tang, J.; Xu, H.; Huang, R.; Chen, Z.; Zhao, Q.; Zhang, Z. Thickness measurement of non-magnetic steel plates using a novel planar triple-coil sensor. NDT & E International, 2019, 107, 102148.
34. Huang, R.; Lu, M.; Peyton, A.; Yin, W. Thickness measurement of metallic plates with finite planar dimension using eddy current method. IEEE Transactions on Instrumentation and Measurement, 2020, 69, 8424-8431.
35. Lu, M.; Meng, X.; Chen, L.; Huang, R.; Yin, W.; Peyton, A. Measurement of ferromagnetic slabs permeability based on a novel planar triple-coil sensor. IEEE Sensors Journal, 2019, 20, 2904-2910.
36. Lu, M.; Zhu, W.; Yin, L.; Peyton, A.; Yin, W.; Qu, Z. Reducing the lift-off effect on permeability measurement for magnetic plates from multifrequency induction data. IEEE Transactions on Instrumentation and Measurement, 2017, 67, 167-174.
37. Lu, M.; Huang, R.; Yin, W.; Zhao, Q.; Peyton, A. Measurement of permeability for ferrous metallic plates using a novel lift-off compensation technique on phase signature. IEEE Sensors Journal, 2019, 19, 7440-7446.
38. Lu, M.; Yin, L.; Peyton, A.; Yin, W. A novel compensation algorithm for thickness measurement immune to lift-off variations using eddy current method. IEEE Transactions on Instrumentation and Measurement, 2016, 65, 2773-2779.
39. Lu, M.; Chen, L.; Meng, X.; Huang, R.; Peyton, A.; Yin, W. Thickness measurement of metallic film based on a high-frequency feature of triple-coil electromagnetic eddy current sensor. IEEE Transactions on Instrumentation and Measurement, 2020, 70, 1-8.
40. Lu, M.; Meng, X.; Huang, R.; Chen, L.; Peyton, A.; Yin, W. Measuring lift-off distance and electromagnetic property of metal using dual-frequency linearity feature. IEEE Transactions on Instrumentation and Measurement, 2020, 70, 1-9.
41. Lu, M.; Meng, X.; Huang, R.; Chen, L.; Peyton, A.; Yin, W. Liftoff tolerant pancake eddy-current sensor for the thickness and spacing measurement of nonmagnetic plates. IEEE Transactions on Instrumentation and Measurement, 2020, 70, 1-9.
42. Huang, R.; Lu, M.; He, X.; Peyton, A.; Yin, W. Measuring Coaxial Hole Size of Finite-Size Metallic Disk Based on a Dual-Constraint Integration Feature Using Multifrequency Eddy Current Testing. IEEE Transactions on Instrumentation and Measurement, 2020, 70, 1-7.
43. W. Zhou, M. Lu, Z. Chen, L. Zhou, L. Yin, Q. Zhao, A. Peyton, Y. Li, W. Yin. "Three-Dimensional Electromagnetic Mixing Models for Dual-Phase Steel Microstructures." Applied Sciences, vol. 8, pp. 529, 2018.
44. M. Lu, et al. "Determination of the magnetic permeability, electrical conductivity, and thickness of ferrite metallic plates using a multi-frequency electromagnetic sensing system," IEEE Transactions on Industrial Informatics, vol. 15, pp. 4111-4119, 2019.
45. R. Huang, M. Lu et al, "Measurement of the radius of metallic plates based on a novel finite region eigenfunction expansion (FREE) method," IEEE Sensors Journal, vol. 20, pp. 15099 – 15106, 2020. Doi: 10.1109/JSEN.2020.3009443.
46. R. Huang, M. Lu et al, "Measuring co-axial hole size of finite-size metallic disk based on a dual-constraint integration feature using multi-frequency eddy current testing," IEEE Transactions on Instrumentation and Measurement, vol. 70, pp. 1-7, 2020. Doi: 10.1109/TIM.2020.3026762.
47. Lu, Mingyang, Xiaobai Meng, Ruochen Huang, Liming Chen, Anthony Peyton, and Wuliang Yin. "Liftoff tolerant pancake eddy-current sensor for the thickness and spacing measurement of nonmagnetic plates." IEEE Transactions on Instrumentation and Measurement 70 (2020): 1-9.

48. Lu, Mingyang, Xiaobai Meng, Ruochen Huang, Liming Chen, Anthony Peyton, and Wuliang Yin. "Inversion of Distance and Magnetic Permeability Based on Material-Independent and Liftoff Insensitive Algorithms Using Eddy Current Sensor." IEEE Transactions on Instrumentation and Measurement 70 (2020): 1-9.
49. W. Yin et al, “Measurements of Thickness for Metallic Plates With Co-Axial Holes Using a Novel Analytical Method With the Modified Integration Range,” IEEE Access, vol. 8, pp. 198301 – 198306, 2020.
50. X. Meng, M. Lu et al, “Inversion of lift-off distance and thickness for non-magnetic metal using eddy current testing,” IEEE Transactions on Instrumentation and Measurement, vol. 70, 2020. Doi: 10.1109/TIM.2020.3038289.
51. Yin, W.; Tang, J.; Lu, M.; et al. An equivalent-effect phenomenon in eddy current non-destructive testing of thin structures. IEEE Access, 2019, 7, pp. 70296-70307.
52. Lu, M.; et al. Determination of Surface Crack Orientation Based on Thin-Skin Regime Using Triple-Coil Drive–Pickup Eddy-Current Sensor. IEEE Transactions on Instrumentation and Measurement, 2020, 70, pp. 1-9. DOI: 10.1109/TIM.2020.3044729
53. M. Lu, et al., "Prediction of the asymptotical magnetic polarization tensors for cylindrical samples using the boundary element method," In 2015 IEEE Sensors Applications Symposium (SAS), pp. 1-4. IEEE, 2015.
54. R. Huang, M. Lu, A. Peyton, and W. Yin, "A novel perturbed matrix inversion based method for the acceleration of finite element analysis in crack-scanning eddy current NDT," IEEE Access, vol. 8, pp. 12438-12444, 2020.
55. J. Tang et al., "A Novel Efficient FEM Thin Shell Model for Bio-Impedance Analysis," Biosensors, vol. 10, no. 6, pp. 69, 2020.
56. L. Chen, et al., "Textile Based Capacitive Sensor for Physical Rehabilitation via Surface Topological Modification," ACS Nano, vol. 14, no. 7, pp. 8191-8201, 2020. DOI: 10.1021/acsnano.0c01643
57. Z. Jin, et al., "Methods of Controlling Lift-off in Conductivity Invariance Phenomenon for Eddy Current Testing," IEEE ACCESS, vol. 8, pp. 2169-3536, 2020. DOI: 10.1109/ACCESS.2020.3007216.
58. J. Tang, et al., "Effect of frozen-thaw injury on cell membrane and bio-impedance," In 2020 IEEE International Instrumentation and Measurement Technology Conference (I2MTC), pp. 1-6. IEEE, 2020.
59. J. Tang, et al., "Bio-impedance spectroscopy for frozen-thaw of bio-samples: Non-contact inductive measurement and finite element (FE) based cell modelling," Journal of Food Engineering, vol. 272, pp. 109784, 2020.
60. H. Xu et al., "Imaging a weld cross-section using a novel frequency feature in multi-frequency eddy current testing," Insight-Non-Destructive Testing and Condition Monitoring, vol. 61, no. 12, pp. 738 - 743, 2019.
61. Y. Xie et al., "Novel Wearable Sensors for Biomechanical Movement Monitoring Based on Electromagnetic Sensing Techniques," IEEE Sensors Journal, vol. 20, no. 2, 2020. DOI: 10.1109/JSEN.2019.2943487
62. W. Yin et al., "Permeability invariance phenomenon and measurement of electrical conductivity for ferrite metallic plates," Insight-Non-Destructive Testing and Condition Monitoring, vol. 61, no. 8, pp. 472 - 479, 2019.
63. M. Lu et al., "A model for the triboelectric nanogenerator with inductive load and its energy boost potential," Nano Energy, vol. 63, pp. 103883, 2019.
64. M. Lu et al., "Forward solver for deep earth exploration and induction logging using custom built Edge-Element FEM technique," Acta Geologica Sinica, vol. 93, pp. 302-304, 2019.
65. L. Chen et al., "Whole System Design of Wearable Magnetic Induction Sensor for Physical Rehabilitation," Advanced Intelligent Systems, vol. 1, no. 1, pp. 1900037, 2019.
66. Y. X et al., "A self-powered radio frequency (RF) transmission system based on the combination of triboelectric nanogenerator (TENG) and piezoelectric element for disaster rescue/relief," Nano Energy, vol. 54, pp. 331-340, 2018.
67. W. Yin et al., "Custom edge-element FEM solver and its application to eddy-current simulation of realistic 2M-element human brain phantom," Bioelectromagnetics, vol. 39, no. 8, pp. 604-616, 2018.
68. L. Yin et al., "Detection of corrosion pits based on an analytically optimised eddy current sensor," Insight-Non-Destructive Testing and Condition Monitoring, vol. 60, no. 10, pp. 561-567, 2018.
69. W. Yin et al., "Acceleration of eddy current computation for scanning probes," Insight-Non-Destructive Testing and Condition Monitoring, vol. 60, no. 10, pp. 547-555, 2018.
70. M. Lu, et al., "Determining the magnetic permeability of ferrite steel strip by a custom inversion method," In Proc. 12th ECNDT, pp. 1-8. 2018.
71. J. Tang, et al., "Cellular structure analysis based on magnetic induction finite element method simulations and measurements," bioRxiv, pp. 275271, 2018. DOI: 10.1101/275271
72. J.R.S. Avila, et al., "A novel dual modality sensor with sensitivities to permittivity, conductivity, and permeability," IEEE Sensors Journal, vol. 18, no. 1, pp. 356-362, 2017.
73. T. Yang, et al., "Level measurement for saline with a small surface area using high frequency electromagnetic sensing technique," Measurement, vol. 101, pp. 118-125, 2017.
74. X. Meng, et al, “Evaluation of coating thickness using lift-off insensitivity of eddy current sensor," Sensors, vol. 21, no. 2, pp. 419, 2021.
75. Meng, X.; Lu, M.; Yin, W.; Bennecer, A.; Kirk, K.J. Evaluation of Coating Thickness Using Lift-Off Insensitivity of Eddy Current Sensor. Sensors 2021, 21, 419. https://doi.org/10.3390/s21020419
76. M. Lu, et al., "Thickness measurement of circular metallic film using single-frequency eddy current sensor," NDT & E International, vol. 119, pp. 102420, 2021.
77. G. Hu, et al., "Measurement of Radius of a Metallic Ball Using Eddy Current Testing Based on Peak Frequency Difference Feature," Measurement, vol. 184, pp. 109876, 2021.
78. Y. Xie, et al., " A novel design of window function modulated meander-line-coils EMATs for unidirectional Rayleigh waves generation and sidelobes suppression," NDT & E International, vol. 123, pp. 102501, 2021.

79. M. Lu, et al., "Lift-off invariant inductance of steels in multi-frequency eddy-current testing." NDT & E International, vol. 121, p. 102458, 2021.
80. Z. Jin, et al., "Boundary-element analysis of magnetic polarization tensor for metallic cylinder." IEEE Access, vol. 9, pp. 63250-63256, 2021
81. M. Lu, et al., " A high-frequency phase feature for the measurement of magnetic permeability using eddy current sensor." NDT & E International, pp. 102519, 2021, ISSN 0963-8695, https://doi.org/10.1016/j.ndteint.2021.102519.
82. Lu, M.; Meng, X.; Huang, R.; Chen, L.; Peyton, A.; Yin, W. A High-Frequency Phase Feature for the Measurement of Magnetic Permeability Using Eddy Current Sensor. Preprints 2021, 2021080154 (doi: 10.20944/preprints202108.0154.v1)
83. Lu, M, Yin, W & Peyton, A 2015, A custom edge-element FEM solver for eddy current NDT. in 54th Annual British Conference of Non-Destructive Testing, NDT 2015. British Institute of Non-Destructive Testing, 54th Annual British Conference of Non-Destructive Testing, Telford, United Kingdom, 8/09/15.
84. Lu, Mingyang, Noushin Karimian, Anthony Peyton, and Wuliang Yin. "Acceleration of Sweeping Frequency in Eddy Current Computation." In 55th Annual Conference of the British Institute of Non-Destructive Testing, pp. 494-507. British Institute of Non-Destructive Testing, 2016.
85. Lu, Mingyang. Forward and inverse analysis for non-destructive testing based on electromagnetic computation methods. The University of Manchester (United Kingdom), 2018.
86. Lu, M. "Inversion analysis of the spectra of a multi-frequency electromagnetic sensor to determine the magnetic permeability, electrical conductivity and thickness of steel strip." Forward and inverse analysis for non-destructive testing based on electromagnetic computation methods: 102.
87. Lu, M. "Conductivity Lift-off Invariance and measurement of permeability for magnetic plates." Forward and inverse analysis for non-destructive testing based on electromagnetic computation methods: 78.
88. Lu, M. "Acceleration of Eddy Current Computation for Scanning Probes." Forward and inverse analysis for non-destructive testing based on electromagnetic computation methods (2018): 34.
89. Zhu, Shuang, Jorge R. Salas Avila, Yang Tao, Yuedong Xie, Anthony J. Peyton, Jialuo Ding, Stewart Williams, Wuliang Yin, and Mingyang Lu. "Measurement of electrical conductivity for metal wires using an electromagnetic sensor." In 57th Annual Conference of the British Institute of Non-Destructive Testing, pp. 40-48. 2018.
90. Lu, Mingyang, Wenqian Zhu, Wuliang Yin, Frenk Van Den Berg, Haibing Yang, and Anthony Peyton. "12th European Conference on Non-Destructive Testing (ECNDT 2018)." In Determining the magnetic permeability of ferrite steel strip by a custom inversion method. 2018.
91. Karimian, Noushin, Mingyang Lu, John W. Wilson, Wuliang Yin, and Anthony J. Peyton. "Defect representation using the electromagnetic tensor formulation for Eddy Current NDT." In 55th Annual Conference of the British Institute of Non-Destructive Testing, pp. 441-450. British Institute of Non-Destructive Testing, 2016.
92. Xie, Yuedong, Jun Long, Pengfei Zhao, Jinkai Chen, Jikui Luo, Zhijie Zhang, Kai Li et al. "A self-powered radio frequency (RF) transmission system based on the combination of triboelectric nanogenerator (TENG) and piezoelectric element for disaster rescue/relief." Nano Energy 54 (2018): 331-340.